



ELSEVIER

Comput. Methods Appl. Mech. Engrg. 127 (1995) 293–314

**Computer methods
in applied
mechanics and
engineering**

Upper bound limit analysis using discontinuous velocity fields

S.W. Sloan*, P.W. Kleeman

Department of Civil Engineering and Surveying, University of Newcastle, NSW 2308, Australia

Received 8 December 1994

Abstract

A new method for computing rigorous upper bounds under plane strain conditions is described. It is based on a linear three-noded triangular element, which has six unknown nodal velocities and a fixed number of unknown plastic multiplier rates, and uses the kinematic theorem to define a kinematically admissible velocity field as the solution of a linear programming problem. Unlike existing formulations, which permit only a limited number of velocity discontinuities whose directions of shearing must be specified a priori, the new formulation permits velocity discontinuities at all edges shared by adjacent triangles and the directions of shearing are found automatically. The variation of the velocity jump along each discontinuity is described by an additional set of four unknowns. All of the unknowns are subject to the constraints imposed by an associated flow rule and the velocity boundary conditions. The objective function corresponds to the dissipated power, or some related load parameter of interest, and is minimised to yield the desired upper bound. Since plastic deformation may occur not only in the discontinuities, but also throughout the triangular elements as well, the method is capable of modelling complex velocity fields accurately and typically produces tight upper bounds on the true limit load. The formulation is applicable to materials whose strength is cohesive-frictional, purely cohesive and uniform, or purely cohesive and linearly varying, and thus, quite general.

The new procedure is very efficient and always requires fewer elements than existing methods to obtain useful upper bound solutions. Moreover, because of the extra degrees of freedom introduced by the discontinuities, the linear elements no longer need to be arranged in a special pattern to model incompressible behaviour accurately.

1. Introduction

The upper bound theorem is a powerful tool for stability analysis and has been widely used in many areas of geotechnical design. It is, however, often difficult to apply to practical problems which typically involve inhomogeneous soil deposits, complicated loadings and complex geometries. General formulations of the upper bound theorem, which use finite elements and linear programming, have been investigated by Anderheggen and Knopfel [1] and Bottero et al. [2]. These methods permit plastic deformation to occur throughout the continuum and inherit all of the advantages of the finite element technique, but have tended to be computationally cumbersome due to the large linear programming problems that they generate. Anderheggen and Knopfel [1], who were concerned primarily with limit analysis of plates, attempted to address this shortcoming by suggesting various solution strategies based on the revised simplex optimisation algorithm. This type of algorithm was also used by Bottero et al. [2], who generalised the method of Anderheggen and Knopfel [1] to include velocity discontinuities in plane strain limit analysis. Although it constituted an important extension, the formulation of Bottero et al. [2] has the disadvantage that the direction of shearing must be specified for each discontinuity a

* Corresponding author. E-mail: cesws@cc.newcastle.edu.au

priori. This precludes the use of a large number of discontinuities in an arbitrary arrangement, since it is generally not possible to determine these directions so that the mode of failure is kinematically acceptable. The revised simplex optimisation procedure used by Bottero et al. [2] also appeared to be rather slow and, indeed, they suggested that a more efficient solution strategy needed to be found.

One very effective means of solving large, sparse linear programming problems is the steepest edge active set scheme. Although it was originally developed for a finite element formulation of the lower bound theorem [3, 4], this scheme is also very efficient for upper bound analysis as well. This is because the form of the dual upper bound linear programming problem is very similar to the form of the lower bound linear programming problem, with more rows than columns in its constraint matrix and all of its variables unrestricted in sign. The advantages of solving the dual of the upper bound linear programming problem by the active set algorithm are discussed fully in Sloan [5], who also gives a detailed numerical description of the various matrices. The active set method is fast, stable and typically arrives at the optimal solution with remarkably few iterations. Because of its modest memory demands, this type of upper bound formulation is suitable for use on a workstation or microcomputer.

When using the linear three-noded element, it is necessary to arrange the grid so that four triangles form a quadrilateral, with the central node lying at the intersection of the diagonals. If this pattern is not used, then the elements cannot provide a sufficient number of degrees of freedom to satisfy the incompressibility condition that accompanies undrained failure, as discussed in detail by Nagtegaal et al. [6]. In response to this shortcoming, Yu et al. [7] developed a quadratic element for upper bound limit analysis. This formulation can be used to model an incompressible velocity field without resorting to special grid arrangements and is also more efficient than an equivalent linear formulation with the same number of nodes. It does, however, suffer from the same shortcomings as the formulation of Bottero et al. [2], in that the direction of shearing for each velocity discontinuity must be specified a priori.

This paper generalises the active set upper bound formulation of Sloan [5] to permit a large number of discontinuities in the velocity field. The method is based on a linear three-noded triangle which has six unknown nodal velocities and a fixed number of unknown plastic multiplier rates. A velocity discontinuity may occur at any edge that is shared by a pair of adjacent triangles, and the sign of shearing is chosen automatically during the optimisation process to give the least amount of dissipated power. Each discontinuity is typically defined by four nodes and requires four unknowns to describe the tangential velocity jumps along its length. To ensure that the computed velocity field is kinematically admissible, the unknowns are subject to constraints which are generated by the flow rule and boundary conditions. A linearised yield criterion is employed to permit these constraints to be expressed as linear equalities, and the objective function corresponds to the power dissipated by plastic shearing in the discontinuities and triangles. Once the solution to the upper bound linear programming problem has been found, a rigorous upper bound on the exact collapse load is found in the usual way by equating the rate of work of the external forces to the rate of dissipation of internal work.

The new formulation is computationally efficient and gives good estimates of the true limit load with a relatively coarse grid. Because of the number of velocity discontinuities that can be incorporated into the analysis, the results are less sensitive to the mesh arrangement than in previous formulations. Indeed, the new technique does not require the elements to be arranged in a special pattern in order to model the incompressibility condition satisfactorily. A number of applications are given to illustrate the utility and effectiveness of the proposed method, and include detailed comparisons with results obtained from other approaches.

2. Formulation

The three-noded triangle used in the upper bound formulation is shown in Fig. 1. Each node has two velocity components and each element has p plastic multiplier rates (where p is the number of planes in the linearised yield criterion). Within a triangle, the velocities are assumed to vary linearly according to

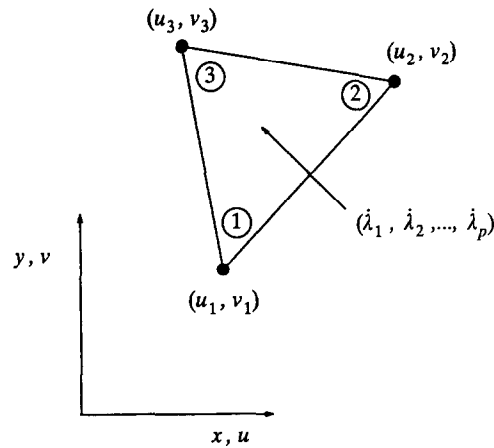


Fig. 1. Triangular element for upper bound limit analysis.

$$u = \sum_{i=1}^{i=3} N_i u_i \quad (1)$$

$$v = \sum_{i=1}^{i=3} N_i v_i \quad (2)$$

where (u_i, v_i) are nodal velocities in the x - and y -directions, respectively, and N_i are linear shape functions. The N_i may be expressed in terms of the nodal coordinates (x_i, y_i) according to

$$N_1 = [(x_2 y_3 - x_3 y_2) + y_{23} x + x_{32} y] / 2A \quad (3)$$

$$N_2 = [(x_3 y_1 - x_1 y_3) + y_{31} x + x_{13} y] / 2A \quad (4)$$

$$N_3 = [(x_1 y_2 - x_2 y_1) + y_{12} x + x_{21} y] / 2A \quad (5)$$

where

$$x_{32} = x_3 - x_2 \quad y_{23} = y_2 - y_3$$

$$x_{13} = x_1 - x_3 \quad y_{31} = y_3 - y_1$$

$$x_{21} = x_2 - x_1 \quad y_{12} = y_1 - y_2$$

and

$$2A = |(x_1 - x_3)(y_2 - y_3) - (x_3 - x_2)(y_3 - y_1)|$$

is twice the triangle area.

2.1. Constraints for plastic flow in continuum

To be kinematically admissible, and thus provide a rigorous upper bound on the exact collapse load, the velocity field must satisfy the set of constraints imposed by an associated flow rule. For plane strain deformation of a rigid plastic soil, the associated flow rule is of the form

$$\dot{\epsilon}_x = \frac{\partial u}{\partial x} = \dot{\lambda} \frac{\partial F}{\partial \sigma_x}$$

$$\dot{\epsilon}_y = \frac{\partial v}{\partial y} = \dot{\lambda} \frac{\partial F}{\partial \sigma_y}$$

$$\dot{\gamma}_{xy} = \left(\frac{\partial v}{\partial x} + \frac{\partial u}{\partial y} \right) = \dot{\lambda} \frac{\partial F}{\partial \tau_{xy}}$$

where $\dot{\lambda} \geq 0$ is a plastic multiplier rate and tensile strains are taken as positive. These equations, together with the boundary conditions and flow rule relations for the velocity discontinuities, define a kinematically admissible velocity field. To remove the stress terms from the rule equations, and thus provide a linear relationship between the unknown velocities and plastic multiplier rates, a linear approximation to the yield surface is employed. This surface must be external to the parent yield surface to ensure that the solution found is a rigorous upper bound on the exact solution. For plane strain loading, the Mohr–Coulomb yield criterion may be written as

$$F = (\sigma_x - \sigma_y)^2 + (2\tau_{xy})^2 - (2c \cos \phi - (\sigma_x + \sigma_y) \sin \phi)^2 = 0$$

where c is the soil cohesion, ϕ is the soil friction angle, and tensile normal stresses are taken as positive. As discussed in Bottero et al. [2], it is convenient to linearise this surface by using a symmetric arrangement of planes in stress space. For an external linearisation with p planes, the equation of the k th plane of the Mohr–Coulomb criterion becomes

$$F_k = A_k \sigma_x + B_k \sigma_y + C_k \tau_{xy} - 2c \cos \phi = 0 \quad (6)$$

where $A_k = \cos a_k + \sin \phi$, $B_k = \sin \phi - \cos a_k$, $C_k = 2 \sin a_k$, $a_k = 2\pi k/p$ and $k = 1, 2, \dots, p$. The number of planes that are required to model the Mohr–Coulomb yield with sufficient accuracy is typically about twelve, although more planes may be necessary for analysis of soils with high friction angles. Note that (6) is also valid for undrained analysis with a Tresca soil model, where c becomes the undrained shear strength, except that F_k , A_k and B_k are computed with $\phi = 0$. Indeed, we assume that the cohesion c may vary linearly with the coordinates (x, y) so as to model the important special case where the undrained shear strength varies linearly with depth.

The flow rule imposes three equality constraints on the nodal velocities and plastic multiplier rates for each element. For the linearised yield criterion defined by (6), the plastic strain rates are given by

$$\dot{\epsilon}_x = \frac{\partial u}{\partial x} = \dot{\lambda} \frac{\partial F}{\partial \sigma_x} = \sum_{k=1}^{k=p} \dot{\lambda}_k \frac{\partial F_k}{\partial \sigma_x} = \sum_{k=1}^{k=p} \dot{\lambda}_k A_k \quad \dot{\lambda}_k \geq 0 \quad (7)$$

$$\dot{\epsilon}_y = \frac{\partial v}{\partial y} = \dot{\lambda} \frac{\partial F}{\partial \sigma_y} = \sum_{k=1}^{k=p} \dot{\lambda}_k \frac{\partial F_k}{\partial \sigma_y} = \sum_{k=1}^{k=p} \dot{\lambda}_k B_k \quad \dot{\lambda}_k \geq 0 \quad (8)$$

$$\dot{\gamma}_{xy} = \left(\frac{\partial v}{\partial x} + \frac{\partial u}{\partial y} \right) = \dot{\lambda} \frac{\partial F}{\partial \tau_{xy}} = \sum_{k=1}^{k=p} \dot{\lambda}_k \frac{\partial F_k}{\partial \tau_{xy}} = \sum_{k=1}^{k=p} \dot{\lambda}_k C_k \quad \dot{\lambda}_k \geq 0 \quad (9)$$

where $\dot{\lambda}_k$ is the non-negative plastic multiplier rate associated with the k th plane of the yield surface. Differentiating Eqs. (1) and (2) with respect to the coordinates and substituting in the above, the flow rule constraints for each triangle may be written as

$$\sum_{i=1}^{i=3} \frac{\partial N_i}{\partial x} u_i - \sum_{k=1}^{k=p} \dot{\lambda}_k A_k = 0 \quad \dot{\lambda}_k \geq 0$$

$$\sum_{i=1}^{i=3} \frac{\partial N_i}{\partial y} v_i - \sum_{k=1}^{k=p} \dot{\lambda}_k B_k = 0 \quad \dot{\lambda}_k \geq 0$$

$$\sum_{i=1}^{i=3} \frac{\partial N_i}{\partial x} v_i + \sum_{i=1}^{i=3} \frac{\partial N_i}{\partial y} u_i - \sum_{k=1}^{k=p} \dot{\lambda}_k C_k = 0 \quad \dot{\lambda}_k \geq 0$$

Substituting Eqs. (3)–(5), the matrix form of these flow rule constraints is

$$a_{11}x_1 - a_{12}x_2 = 0 \tag{10}$$

where

$$a_{11} = \frac{1}{2A} \begin{bmatrix} y_{23} & 0 & y_{31} & 0 & y_{12} & 0 \\ 0 & x_{32} & 0 & x_{13} & 0 & x_{21} \\ x_{32} & y_{23} & x_{13} & y_{31} & x_{21} & y_{12} \end{bmatrix} \quad x_1 = \begin{Bmatrix} u_1 \\ v_1 \\ u_2 \\ v_2 \\ u_3 \\ v_3 \end{Bmatrix}$$

$$a_{12} = \begin{bmatrix} A_1 & A_2 & A_3 & \dots & A_k & \dots & A_p \\ B_1 & B_2 & B_3 & \dots & B_k & \dots & B_p \\ C_1 & C_2 & C_3 & \dots & C_k & \dots & C_p \end{bmatrix} \quad x_2 = \begin{Bmatrix} \lambda_1 \\ \lambda_2 \\ \vdots \\ \lambda_k \\ \vdots \\ \lambda_p \end{Bmatrix}$$

and there are p inequality constraints on the plastic multipliers of the form

$$x_2 \geq 0$$

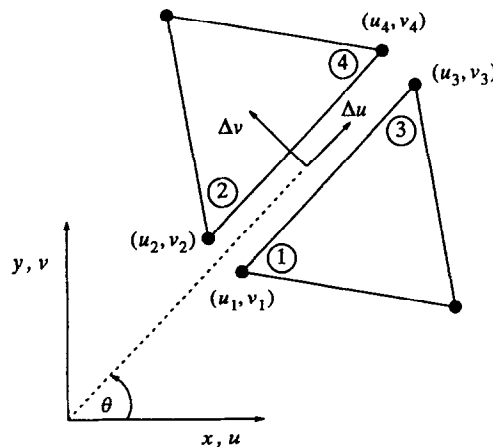
The flow rule constraints defined by (10) must be satisfied by every triangle in the mesh.

2.2. Constraints for plastic flow in velocity discontinuities

The method for incorporating an arbitrary arrangement of velocity discontinuities in the new upper bound formulation is not obvious, and is the major contribution of this paper. The key idea is that the formulation permits the flow rule in the discontinuities to be violated, but does so in a manner that preserves the upper bound property of the solution.

A typical velocity discontinuity is shown in Fig. 2. The discontinuity occurs at the common edge between two adjacent triangles, defined by the nodal pairs (1, 2) and (3, 4), and is of zero thickness. To be kinematically admissible, the normal and tangential velocity jumps across the discontinuity must satisfy the flow rule, which for a Mohr–Coulomb yield criterion is of the form

$$\Delta v = |\Delta u| \tan \phi \tag{11}$$



$$\Delta u_{ij} = (u_j - u_i) \cos \theta + (v_j - v_i) \sin \theta$$

$$\Delta v_{ij} = (u_i - u_j) \sin \theta + (v_j - v_i) \cos \theta$$

Fig. 2. Velocity discontinuity geometry.

where Δv is the normal velocity jump and Δu is the tangential velocity jump. The absolute value on the right-hand side of this equation is necessary because, for a non-zero friction angle, dilation occurs regardless of the sign of tangential shearing. For any pair of nodes on the discontinuity (i, j), the tangential and normal velocity jumps are defined in terms of the Cartesian nodal velocities by the relations

$$\Delta u_{ij} = (u_j - u_i) \cos \theta + (v_j - v_i) \sin \theta \tag{12}$$

$$\Delta v_{ij} = (u_i - u_j) \sin \theta + (v_i - v_j) \cos \theta \tag{13}$$

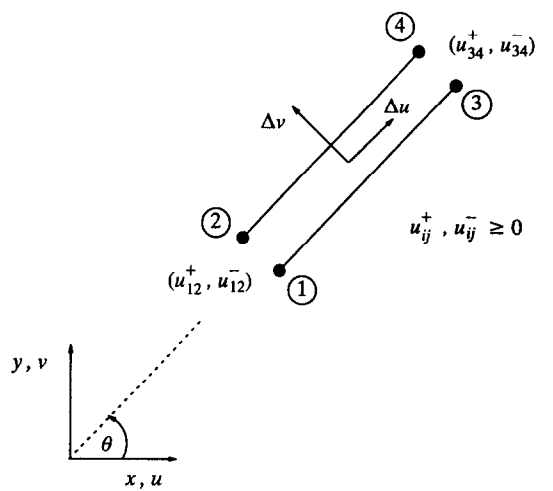
where θ is the angle of the discontinuity to the x -axis. One possible method for imposing the flow constraints on the velocity field is to simply enforce (11) at each pair of nodes using Eqs. (12) and (13). Since the velocities vary linearly, this guarantees that the flow rule is satisfied at every point on the discontinuity. The drawback with this approach is that the absolute value sign prevents the upper bound formulation being cast as a standard linear programming problem. To avoid this shortcoming, Bottero et al. [2] and later, Sloan [5], specified a sign condition so that $s \Delta u$ replaces $|\Delta u|$ where $s = \pm 1$. This method enables the linear programming formulation to be preserved, but has the disadvantage that it requires additional constraints of the form

$$s \Delta u_{ij} \geq 0$$

to be imposed at each nodal pair (i, j) on the discontinuity. These constraints limit the range of kinematically admissible solutions unnecessarily and, because of the difficulty in specifying the correct sign of the tangential velocity jump a priori, also severely restrict the number of discontinuities that can be used in practical calculations [8–10]. A formulation which permits an arbitrary number of velocity discontinuities with unprescribed signs is clearly desirable, and this need was the motivation for the current work.

In the proposed formulation, each nodal pair (i, j) on a discontinuity is associated with two non-negative variables u_{ij}^+ and u_{ij}^- , as shown in Fig. 3, and thus gives rise to two additional unknowns. The tangential velocity jump at each nodal pair Δu_{ij} is defined as the difference between these two quantities according to

$$\Delta u_{ij} = u_{ij}^+ - u_{ij}^- \tag{14}$$



$$\Delta u_{ij} = u_{ij}^+ - u_{ij}^- = (u_j - u_i) \cos \theta + (v_j - v_i) \sin \theta$$

$$\Delta v_{ij} = (u_{ij}^+ + u_{ij}^-) \tan \phi$$

Fig. 3. Velocity discontinuity variables.

Each discontinuity thus gives rise to a total of four equality constraints on the parameters x_1 and x_3 , with the latter also being subject to four inequality constraints.

The substitution made in Eq. (11), where $|\Delta u|$ is replaced by $(u^+ + u^-)$ instead of $|u^+ - u^-|$, is clearly inexact if u^+ and u^- are both positive simultaneously. Thus, the correct flow rule is satisfied only if either $u^+ = 0$ or $u^- = 0$ at both nodes of the discontinuity. If this is not the case, it is possible to prove that the discontinuity behaves as though it were in a soil of greater strength, with c^* and ϕ^* such that $c^* \geq c$, $\phi^* \geq \phi$ and $c^* \cot \phi^* = c \cot \phi$. This key result, which is proved in the Appendix, guarantees that the new formulation will yield a rigorous upper bound on the true collapse load for a soil whose strength parameters are c and ϕ . It is perhaps worth remarking at this point that the correct flow rule of (11) always appears to be satisfied precisely in actual computations with the proposed procedure, but there is no direct way of proving that this will always be the case.

Note that the special case of a purely cohesive material is modelled simply by substituting $\phi = 0$ in (23). This ensures that the normal velocity jump is zero at both ends of the discontinuity (and therefore zero at every point along its length), and guarantees that plastic flow occurs at constant volume.

2.3. Velocity boundary conditions

To be kinematically admissible, the computed velocity field must satisfy the prescribed boundary conditions. Consider a node i on a boundary which is inclined at an angle θ to the x -axis. For the general case, where the boundary is subject to a prescribed tangential velocity \bar{u} and a prescribed normal velocity \bar{v} , the nodal velocity components (u_i, v_i) must satisfy the equalities

$$\begin{bmatrix} \cos \theta & \sin \theta \\ -\sin \theta & \cos \theta \end{bmatrix} \begin{Bmatrix} u_i \\ v_i \end{Bmatrix} = \begin{Bmatrix} \bar{u} \\ \bar{v} \end{Bmatrix}$$

These constraints may be expressed in matrix form as

$$a_{31} x_1 = b_3 \tag{24}$$

where

$$a_{31} = \begin{bmatrix} \cos \theta & \sin \theta \\ -\sin \theta & \cos \theta \end{bmatrix} \quad x_1 = \begin{Bmatrix} u_i \\ v_i \end{Bmatrix} \quad b_3 = \begin{Bmatrix} \bar{u} \\ \bar{v} \end{Bmatrix}$$

The above type of velocity boundary condition may be used to define the ‘loading’ caused by a stiff structure, such as a rigid strip footing or retaining wall. For problems where part of the body is loaded by a uniform normal pressure, such as a flexible strip footing, it is often convenient to impose constraints on the surface normal velocities of the form

$$\int_S \bar{v} \, dS = Q \tag{25}$$

In the above, Q is a prescribed rate of flow of material across the boundary S and is typically set to unity. This type of constraint, when substituted into the power expended by the external loads, permits an applied uniform pressure to be minimised directly. Since the velocities vary linearly, (25) may be expressed in terms of the nodal velocities according to

$$\frac{1}{2} \sum_{\text{edges}} [(v_i + v_j) \cos \theta_{ij} - (u_i + u_j) \sin \theta_{ij}] l_{ij} = Q$$

where l_{ij} and θ_{ij} denote the length and inclination of each segment on S and each segment is defined by the end nodes (i, j) . This boundary condition may be written in matrix form as

$$a_{41} x_1 = b_4 \tag{26}$$

where

$$\mathbf{a}_{41} = \frac{1}{2} [-l_{12} \sin \theta_{12} \quad l_{12} \cos \theta_{12} \quad -l_{12} \sin \theta_{12} \quad l_{12} \cos \theta_{12} \quad \dots] \quad \mathbf{x}_1 = \begin{Bmatrix} u_1 \\ v_1 \\ u_2 \\ v_2 \\ \vdots \end{Bmatrix} \quad \mathbf{b}_4 = \{Q\}$$

Another type of constraint, which is not strictly a boundary condition, arises when a body is subjected to loading by gravity. In this case, it is sometimes convenient to constrain the vertical velocity field so that

$$\sum_{\text{triangles}} \iint_A v \, dA = -W \quad (27)$$

where W is a prescribed constant which is typically set to unity. This constraint permits the unit weight γ to be minimised directly when the power expended by the external loads is equated to the internal power dissipation and is useful, for example, when analysing the behaviour of slopes. Noting that

$$\int_A v \, dA = \frac{A}{3} (v_1 + v_2 + v_3) \quad (28)$$

for each triangle, the constraint of Eq. (27) may be written as

$$\mathbf{a}_{51} \mathbf{x}_1 = \mathbf{b}_5 \quad (29)$$

where

$$\mathbf{a}_{51} = \frac{1}{3} [0 \quad A_1 \quad 0 \quad A_1 \quad 0 \quad A_1 \quad \dots] \quad \mathbf{x}_1 = \begin{Bmatrix} u_1 \\ v_1 \\ u_2 \\ v_2 \\ u_3 \\ v_3 \\ \vdots \end{Bmatrix} \quad \mathbf{b}_5 = \{-W\}$$

2.4. Power dissipation in continuum

A key feature of the formulation is that plastic flow may occur in both the continuum and the velocity discontinuities. The total power dissipated in these modes constitutes the objective function and is expressed in terms of the unknowns. Within each triangle, the power dissipated by the plastic stresses is given by

$$P_c = \int_A (\sigma_x \dot{\epsilon}_x + \sigma_y \dot{\epsilon}_y + \tau_{xy} \dot{\gamma}_{xy}) \, dA$$

After substituting Eqs. (7)–(9) and collecting terms, this dissipation may also be expressed as

$$P_c = 2A \cos \phi \sum_{k=1}^{k=p} \dot{\lambda}_k \int_A c \, dA$$

If we assume that the cohesion varies linearly throughout the triangle, this integral may be evaluated analytically to give

$$P_c = \mathbf{c}_2^T \mathbf{x}_2 \quad (30)$$

where

$$\mathbf{c}_2^T = \frac{2}{3} A (c_1 + c_2 + c_3) \cos \phi [1 \quad 1 \quad \dots \quad 1] \quad \mathbf{x}_2 = \begin{Bmatrix} \dot{\lambda}_1 \\ \dot{\lambda}_2 \\ \vdots \\ \dot{\lambda}_p \end{Bmatrix}$$

and c_1, c_2, c_3 are nodal values of the cohesion. Since the plastic multiplier rates are constrained so that $\mathbf{x}_2 \geq \mathbf{0}$, it follows that the power dissipated in each triangle is non-negative.

2.5. Power dissipation in velocity discontinuities

The power dissipated by plastic shearing along a velocity discontinuity is given by an integral of the form

$$\int_l c |\Delta u| dl$$

For the discontinuity shown in Fig. 3, the correct expression for the power dissipation is obtained by substituting $|u^+ - u^-|$ for the tangential velocity jump $|\Delta u|$, where u^+ and u^- are defined by Eqs. (18) and (19). In the proposed formulation, however, $(u^+ + u^-)$ is substituted for $|\Delta u|$ in order to preserve the linear character of the objective function according to

$$P_d = \int_l c(u^+ + u^-) dl \quad (31)$$

After substituting (18) and (19) and integrating, the power dissipated in each discontinuity may be written as

$$P_d = \mathbf{c}_3^T \mathbf{x}_3 \quad (32)$$

where

$$\mathbf{c}_3^T = l \left[\frac{1}{3} c_1 + \frac{1}{6} c_2 \quad \frac{1}{3} c_1 + \frac{1}{6} c_2 \quad \frac{1}{6} c_1 + \frac{1}{3} c_2 \quad \frac{1}{6} c_1 + \frac{1}{3} c_2 \right] \quad \mathbf{x}_3 = \begin{Bmatrix} u_{12}^+ \\ u_{12}^- \\ u_{34}^+ \\ u_{34}^- \end{Bmatrix}$$

and the cohesion varies linearly so that c_1 and c_2 are the cohesions at the nodal pairs (1, 2) and (3, 4), respectively. Note that this form of power dissipation is also non-negative, since the discontinuity variables are constrained so that $\mathbf{x}_3 \geq \mathbf{0}$.

3. Assembly and solution of linear programming problem

The constraints that need to be imposed on the unknowns are given by Eqs. (10), (23), (24), (26) and (29). The objective function coefficients for each triangle and discontinuity, which describe the internal power dissipation, are summarised by Eqs. (30) and (32). All of these node and element coefficients may be assembled in the usual manner to give the following linear programming problem

$$\begin{aligned} \text{Minimise} \quad & \mathbf{C}_2^T \mathbf{X}_2 + \mathbf{C}_3^T \mathbf{X}_3 \\ \text{Subject to} \quad & \mathbf{A}_{11} \mathbf{X}_1 + \mathbf{A}_{12} \mathbf{X}_2 = \mathbf{0} \\ & \mathbf{A}_{21} \mathbf{X}_1 + \mathbf{A}_{23} \mathbf{X}_3 = \mathbf{0} \\ & \mathbf{A}_{31} \mathbf{X}_1 = \mathbf{B}_3 \\ & \mathbf{A}_{41} \mathbf{X}_1 = \mathbf{B}_4 \\ & \mathbf{A}_{51} \mathbf{X}_1 = \mathbf{B}_5 \\ & \mathbf{X}_2 \geq \mathbf{0} \\ & \mathbf{X}_3 \geq \mathbf{0} \end{aligned} \quad (33)$$

where \mathbf{X}_1 is a global vector of nodal velocities, \mathbf{X}_2 is a global vector of element plastic multiplier rates, and \mathbf{X}_3 is a global vector of discontinuity parameters. To solve this type of optimisation problem

efficiently, the characteristics of a typical constraint matrix need to be examined so that any of its special features may be exploited.

Consider a grid with N_n nodes, N_t triangles, N_d discontinuities, and p planes in the linearised yield surface where velocity discontinuities occur at all edges that are shared by adjacent triangles. This will give rise to $2N_n$ nodal velocities, pN_t element plastic multiplier rates, and $4N_d$ discontinuity parameters. Since each node is unique to a particular triangle, $N_n = 3N_t$ and the total number of variables is equal to $(6 + p)N_t + 4N_d$. Ignoring the constraints that are generated by the boundary conditions, which are generally small in number, the flow rule relations in the triangles and discontinuities give a total of $3N_t + 4N_d$ equality constraints. This implies that the ratio of variables to constraints in the overall linear programming problem may be predicted by the approximation

$$\frac{n}{m} = \frac{\text{number of columns}}{\text{number of rows}} \approx \frac{(6 + p)N_t + 4N_d}{3N_t + 4N_d} \quad (34)$$

Now, Euler's theorem for a planar triangulation states that the number of discontinuities may be expressed in terms of the number of triangles, the number of unique node coordinates N_c , and the number of boundary edges N_b according to

$$N_d = N_t + N_c - N_b - 1$$

Substituting the well-known result that

$$N_c \approx \frac{1}{2} N_t \quad (35)$$

for a refined mesh [6] where $N_b \ll N_d$, it follows that

$$N_d \approx \frac{3}{2} N_t \quad (36)$$

and (34) becomes

$$\frac{n}{m} \approx \frac{p + 12}{9} \quad (37)$$

Thus, for a refined mesh, the ratio of columns to rows in the overall constraint matrix is essentially dependent on the number of planes that are used to linearise the yield surface. For $p = 6$ the ratio of columns to rows is approximately 2, whilst for $p = 24$, the ratio approaches 4. Typical values for p are in the range 12–24, and for practical computations the overall constraint matrix has at least twice as many columns as rows.

If we again consider the limiting case of a refined mesh, and count the non-zeros in the matrices defined by Eqs. (10) and (23), it is straightforward to show that the density of the overall constraint matrix is predicted approximately by the expression

$$\text{density} = \frac{\text{number of non-zeros}}{\text{number of rows} \times \text{number of columns}} \approx \frac{p + 16}{3N_t(p + 12)} \quad (38)$$

For a grid with $N_t = 300$ and $p = 12$, which is a typical configuration in practice, we observe that the constraint matrix is very sparse with a density of about 0.0013. It is important to note that the degree of this sparsity increases as the number of elements increases.

To express the upper bound linear programming problem in a form which is suitable for solution by the revised simplex method, the unbounded velocities are replaced by making the standard substitution

$$X_1 = X_1^+ - X_1^-$$

with the bound constraints $X_1^+ \geq 0$ and $X_1^- \geq 0$. This permits (33) to be written in the standard form

$$\begin{aligned} &\text{Minimise} && C^T X \\ &\text{Subject to} && AX = B \\ &&& X \geq 0 \end{aligned} \quad (39)$$

where

$$A = \begin{bmatrix} A_{11} & -A_{11} & A_{12} & 0 \\ A_{21} & -A_{21} & 0 & A_{23} \\ A_{31} & -A_{31} & 0 & 0 \\ A_{41} & -A_{41} & 0 & 0 \\ A_{51} & -A_{51} & 0 & 0 \end{bmatrix} \quad X = \begin{Bmatrix} X_1^+ \\ X_1^- \\ X_2 \\ X_3 \end{Bmatrix} \quad B = \begin{Bmatrix} 0 \\ 0 \\ B_3 \\ B_4 \\ B_5 \end{Bmatrix} \quad C = \begin{Bmatrix} 0 \\ 0 \\ C_2 \\ C_3 \end{Bmatrix}$$

Since the overall constraint matrix always has fewer rows than columns, this approach will be reasonably efficient provided appropriate factorisation routines are used to take full account of the inherent sparsity [11, 12].

As an alternative to the revised simplex scheme, it is possible to employ the steepest edge active set algorithm [4] to solve the dual of (33). This approach has been used successfully in a previous formulation of the upper bound theorem [5], and has the advantage that it also provides a very effective solution strategy for a numerical formulation of the lower bound theorem [3]. The active set scheme is suited to sparse linear programming problems where most of the variables are unbounded and there are more rows than columns in the constraint matrix. The steepest edge search greatly reduces the number of iterations that are required to isolate the optimal solution vector in the active set method and, unlike an equivalent scheme for the revised simplex procedure [13], always leads to significant reductions in the total computation time. In its simplest form, the dual of the linear programming problem defined by (33) may be written as

$$\begin{aligned} \text{Minimise} \quad & -B_3^T Z_3 - B_4^T Z_4 - B_5^T Z_5 \\ \text{Subject to} \quad & A_{11}^T Z_1 + A_{21}^T Z_2 + A_{31}^T Z_3 + A_{41}^T Z_4 + A_{51}^T Z_5 = 0 \\ & A_{12}^T Z_1 \leq C_2 \\ & A_{23}^T Z_2 \leq C_3 \end{aligned} \tag{40}$$

where the Z_i are unknown dual variables. This system can be expressed in standard form for the active set method according to

$$\begin{aligned} \text{Minimise} \quad & C^T X \\ \text{Subject to} \quad & A_1 X = B_1 \\ & A_2 X \leq B_2 \end{aligned} \tag{41}$$

where

$$A_1 = [A_{11}^T \quad A_{21}^T \quad A_{31}^T \quad A_{41}^T \quad A_{51}^T] \quad X = \begin{Bmatrix} Z_1 \\ Z_2 \\ Z_3 \\ Z_4 \\ Z_5 \end{Bmatrix} \quad B_1 = \{0\} \\ A_2 = \begin{bmatrix} A_{12}^T & 0 & 0 & 0 & 0 \\ A_{23}^T & 0 & 0 & 0 & 0 \end{bmatrix} \quad B_2 = \begin{Bmatrix} C_2 \\ C_3 \end{Bmatrix} \quad C = \begin{Bmatrix} 0 \\ 0 \\ -B_3 \\ -B_4 \\ -B_5 \end{Bmatrix}$$

After (40) is solved for the dual variables Z_i , it is straightforward to recover the solution to the primal linear programming problem defined by (33). The efficiency of this type of strategy is verified in a later section of the paper.

4. Numerical examples

In this section, the performance of the new upper bound formulation is assessed by using it to predict the collapse load for a plane strain strip footing. Since the exact collapse load for this case is known, it

provides a useful check on the ability of the new method to provide accurate upper bounds. To ascertain the influence of large numbers of discontinuities in the velocity field, the solutions from the new method are compared with those from identical meshes which have no velocity discontinuities. As mentioned previously, a significant advantage of the new scheme is that the triangular elements do not have to be arranged in a special pattern (where four triangles form a quadrilateral with the central node lying at the intersection of the diagonals) to satisfy the incompressibility condition which is implicit in undrained deformation. This point is illustrated by example.

4.1. *Undrained loading of a smooth rigid strip footing*

The exact collapse pressure q_f for a smooth rigid strip footing on a purely cohesive soil may be expressed as $q_f = N_c c_u$, where c_u is the undrained shear strength and the bearing capacity factor $N_c = 2 + \pi$. Two different meshes, one coarse and one fine, are used to analyse this problem with the new procedure and are shown in Fig. 4. The corresponding results are given in Table 1.

Even with a very coarse grid and a crude approximation to the Tresca yield surface ($p = 6$), the new upper bound procedure gives a good estimate of the exact collapse pressure with an error of about 4.9%. As the yield surface approximation is refined by increasing p to 24, the error in the collapse pressure is reduced to a value of 2.1%. The effects of the yield surface linearisation on the collapse load error, for coarse mesh 1, are shown in Fig. 5. These results suggest that, for analysis of purely cohesive soils, the linearisation error is negligible provided at least 18 planes are used to approximate the yield function. For practical computations, a 12 plane approximation should suffice. The results in Table 1

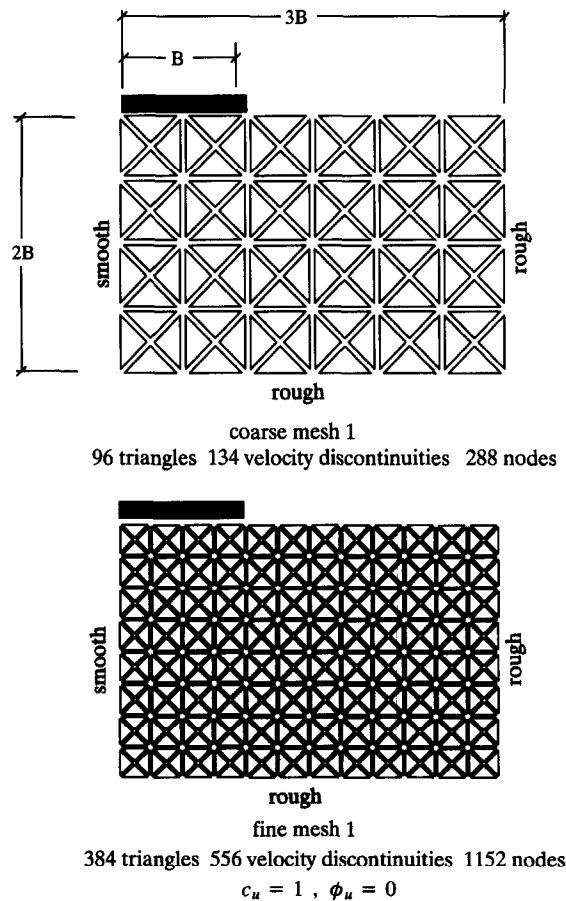


Fig. 4. Meshes for smooth rigid strip footing on purely cohesive soil (four-triangle incompressible mesh pattern with velocity discontinuities).

Table 1

Results for smooth rigid strip footing on purely cohesive layer (four-triangle mesh pattern with velocity discontinuities)

Mesh	p	m	n	i	t (s)	N_c	N_c error (%)
Coarse mesh 1	6	1688	876	488	37	5.39	4.9
Fine mesh 1	6	6832	3480	2060	704	5.38	4.7
Coarse mesh 1	12	2264	876	493	38	5.29	2.9
Fine mesh 1	12	9136	3480	2768	942	5.25	2.1
Coarse mesh 1	24	3416	876	564	46	5.25	2.1
Fine mesh 1	24	13744	3480	3244	1144	5.21	1.4

p = number of planes in linearised yield surface, m = number of rows in constraint matrix, n = number of columns in constraint matrix, i = number of iterations to solve LP, t = CPU time for SUN IPX with f77-O4.

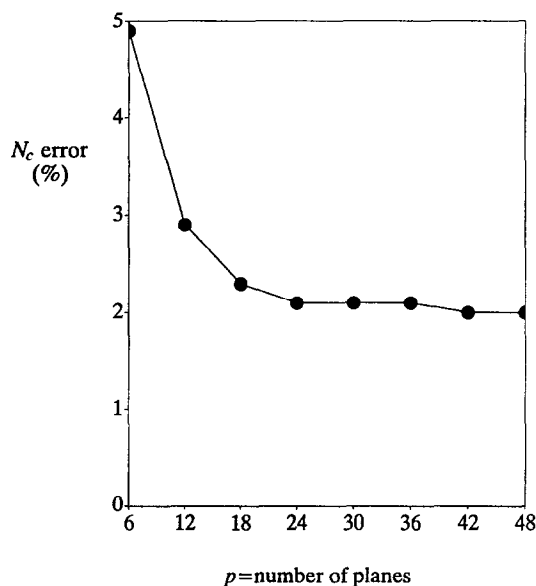


Fig. 5. Effect of yield surface linearisation on collapse load error (coarse mesh 1, smooth rigid strip footing on purely cohesive soil).

also indicate that the collapse loads predicted by the new procedure are not particularly sensitive to the mesh refinement. Although coarse mesh 1 has only 96 triangles and 134 velocity discontinuities, it predicts collapse loads that are almost as accurate as those from the fine mesh, which has 384 triangles and 556 velocity discontinuities. It should be noted that the accuracy of the solution would be further improved by arranging the elements in a fan around the edge of the footing; indeed, if the elements were placed so that the Prandtl collapse mechanism could be reproduced precisely when the exact solution could be approximated very closely. It was decided not to do this in the present work, however, since it is of more interest to know the accuracy of the new method when the exact solution is unknown and a naive mesh is used. In most practical applications, simple grid arrangements such as those in Fig. 4 are usually employed.

Table 2 presents results for runs without velocity discontinuities which were obtained using the meshes shown in Fig. 6. These grids are identical to those in Fig. 4 except they do not include any velocity discontinuities. Not surprisingly, the collapse loads predicted from these meshes are much less accurate than those predicted from equivalent meshes with discontinuities at each of the triangle edges. With no velocity discontinuities and an accurate linearisation of the Tresca yield surface, coarse mesh 2 overpredicts the collapse load by 19.1%. This error is reduced to 9.3% for fine mesh 2 with the same yield surface linearisation. Since the linear programming problems for meshes with velocity discontinuities are larger than those for meshes without velocity discontinuities, the increased accuracy associated with the former is obtained at the cost of increased CPU time. Generally speaking, however,

Table 2
Results for smooth rigid strip footing on purely cohesive layer (four-triangle mesh pattern, no velocity discontinuities)

Mesh	p	m	n	i	t (s)	N_c	N_c error (%)
Coarse mesh 2	6	694	317	212	5.5	6.49	26.3
Fine mesh 2	6	2730	1207	987	96	5.94	15.6
Coarse mesh 2	12	1270	317	296	7.7	6.18	20.2
Fine mesh 2	12	5034	1207	1495	153	5.68	10.5
Coarse mesh 2	24	2422	317	378	12	6.12	19.1
Fine mesh 2	24	9642	1207	1810	210	5.62	9.3

p = number of planes in linearised yield surface, m = number of rows in constraint matrix, n = number of columns in constraint matrix, i = number of iterations to solve LP, t = CPU time for SUN IPX with f77-O4.

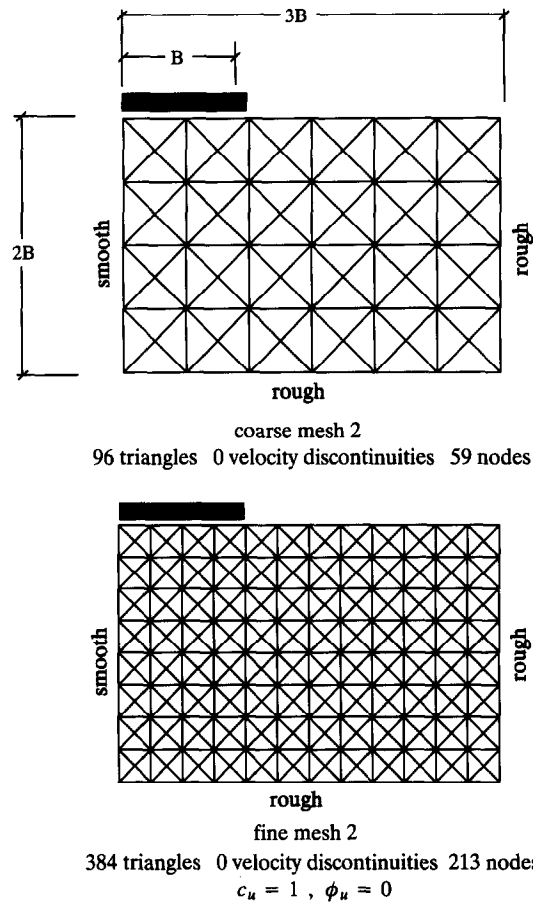


Fig. 6. Meshes for smooth rigid strip footing on purely cohesive soil (four-triangle incompressible mesh pattern, no velocity discontinuities).

the extra cost incurred by the inclusion of discontinuities is balanced by the increase in the accuracy of the limit load. In the case of the coarse mesh with a 24-plane linearisation of the yield surface, for example, the CPU time is increased four-fold but the error in the collapse load is reduced nine-fold. In comparing the relative efficiencies of the two approaches, it should be stressed that all of the analyses may be run easily on a workstation or microcomputer.

As mentioned previously, the solution to the upper bound linear programming problem defines a kinematically admissible velocity field. One such velocity field, for the case of the fine mesh with velocity discontinuities, is shown in Fig. 7. The mode of failure is quite clearly similar, although not identical, to that predicted by the well-known Prandtl mechanism. The velocity field for the fine mesh

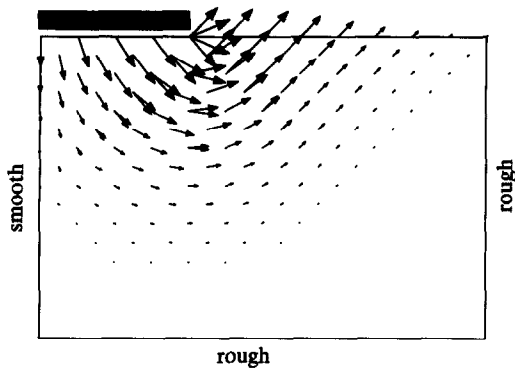


Fig. 7. Velocity vectors for smooth rigid strip footing on purely cohesive soil (fine mesh 1, velocity discontinuities, $p = 24$).

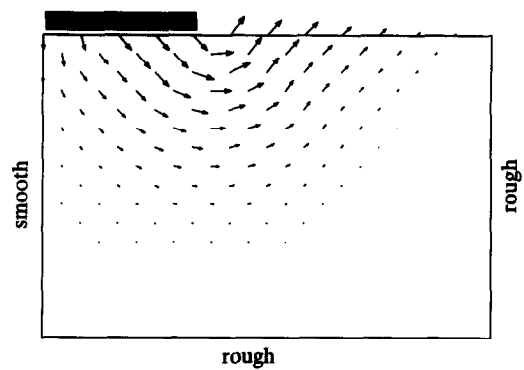


Fig. 8. Velocity vectors for smooth rigid strip footing on purely cohesive soil (fine mesh 2, no velocity discontinuities, $p = 24$).

without discontinuities, shown in Fig. 8, is more constrained in the vicinity of footing due to the requirements of velocity continuity.

For analysis of undrained loading with no velocity discontinuities, the three-noded triangle must be arranged so that four triangles form a quadrilateral with the central node lying at the intersection of the diagonals (as shown in Fig. 6). This important result is a consequence of the incompressibility condition and was first discussed in the context of displacement finite elements by Nagtegaal et al. [6]. They

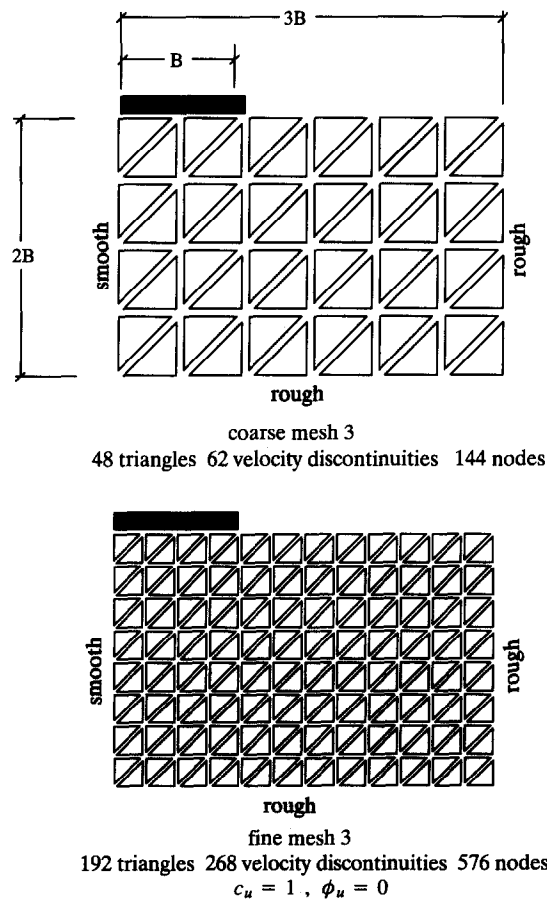


Fig. 9. Meshes for smooth rigid strip footing on purely cohesive soil (two-triangle mesh pattern).

proved that unless this special arrangement is observed, the number of incompressibility constraints exceeds the number of degrees of freedom, even for very fine meshes, and leads to inaccurate solutions. Fig. 9 illustrates coarse and fine meshes of three-noded triangles which are not arranged in the four-triangle pattern, but have velocity discontinuities at all common edges between triangles. The results from these two-triangle mesh configurations, shown in Table 3, indicate that the new formulation predicts reasonably accurate limit loads, despite the fact that the special incompressible mesh pattern is not used. For a 24-plane linearisation of the yield surface, the coarse and fine meshes give very similar estimates of the collapse load, with errors of 4.3% and 3.5%, respectively. The good performance of these meshes is due to the presence of the discontinuities, which introduce additional degrees of freedom and thus permit the velocity field to deform at constant volume. Further evidence of this is the velocity field for the fine mesh, shown in Fig. 10, which is again similar to that predicted by the Prandtl mechanism. To check the predictions of Nagtegaal et al. [6], the fine mesh shown in Fig. 9 was used again but without the velocity discontinuities. The corresponding linear programming problem could not be solved, as the mesh exhibited locking and indicated an infinite collapse load. This feature occurs regardless of the mesh refinement and verifies the analysis of Nagtegaal et al. [6].

4.2. Drained loading of a smooth rigid strip footing

The Prandtl collapse pressure for a surface footing on a weightless cohesive-frictional soil is $q_f = N_c c'$, where $N_c = [\exp(\pi \tan \phi') \tan^2(\pi/4 + \phi'/2) - 1] \cot \phi'$ and c' and ϕ' are, respectively, the effective cohesion and friction angle. The upper bound meshes used to analyse this problem are shown in Fig. 11 with the corresponding results listed in Table 4. All of the results are for a friction angle of 30° , so the exact solution for N_c is 30.14.

Although the collapse predictions for the cohesive-frictional footing are less accurate than those for the purely cohesive footing, they are still sufficiently precise for practical applications. For the coarse

Table 3
Results for smooth rigid strip footing on purely cohesive layer (two-triangle mesh pattern with velocity discontinuities)

Mesh	p	m	n	i	t (s)	N_c	N_c error (%)
Coarse mesh 3	6	824	442	165	5.7	5.59	8.7
Fine mesh 3	6	3376	1750	845	138.9	5.51	7.2
Coarse mesh 3	12	1112	442	195	7.5	5.39	4.9
Fine mesh 3	12	4528	1750	914	158.6	5.36	4.2
Coarse mesh 3	24	1688	442	273	9.6	5.36	4.3
Fine mesh 3	24	6832	1750	1333	198.6	5.32	3.5

p = number of planes in linearised yield surface, m = number of rows in constraint matrix, n = number of columns in constraint matrix, i = number of iterations to solve LP, t = CPU time for SUN IPX with f77-O4.

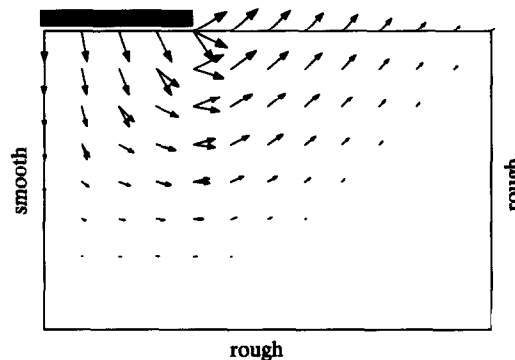


Fig. 10. Velocity vectors for smooth rigid strip footing on purely cohesive soil (fine mesh 3, velocity discontinuities, $p = 24$).

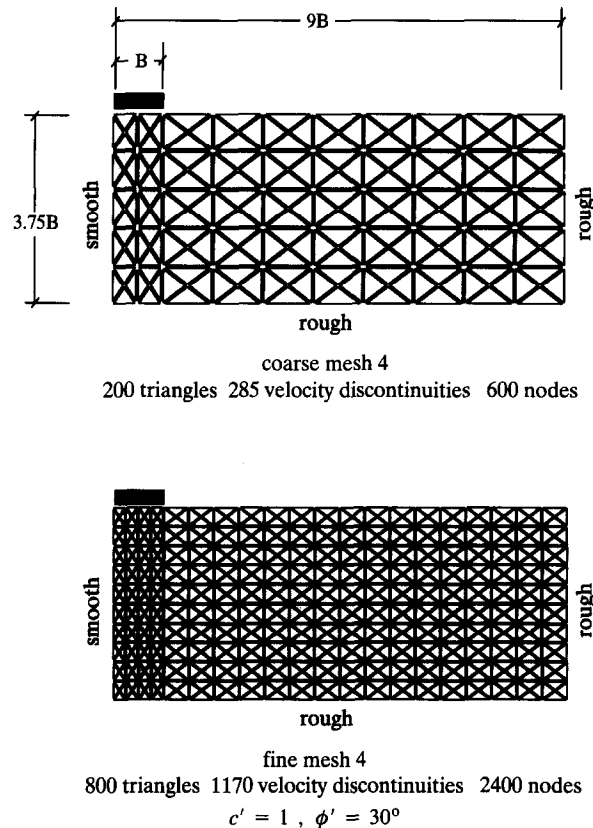


Fig. 11. Meshes for smooth rigid strip footing on cohesive-frictional soil (with velocity discontinuities).

Table 4

Results for smooth rigid strip footing on cohesive-frictional layer (with velocity discontinuities)

Mesh	p	m	n	i	t (s)	N_c	N_c error (%)
Coarse mesh 4	6	3540	1814	1061	220	37.26	23.6
Fine mesh 4	6	14280	7228	4287	4983	37.04	22.9
Coarse mesh 4	12	4740	1814	1008	204	33.36	10.7
Fine mesh 4	12	19080	7228	5805	6900	32.67	8.4
Coarse mesh 4	24	7140	1814	1357	281	32.70	8.5
Fine mesh 4	24	28680	7228	7862	8906	31.75	5.4

p = number of planes in linearised yield surface, m = number of rows in constraint matrix, n = number of columns in constraint matrix, i = number of iterations to solve LP, t = CPU time for SUN IPX with f77-O4.

grid with a crude approximation to the Mohr–Coulomb yield surface ($p = 6$), the new upper bound procedure overestimates the exact collapse pressure by 23.6%. Since this error is reduced to 8.5% when p is increased to 24, the results suggest that the influence of the yield surface approximation is quite pronounced for cohesive-frictional soils with significant friction angles. Indeed, the effect of the yield surface linearisation on the collapse load error, shown in Fig. 12, suggests that a minimum of 18 planes should be used for a soil with a friction angle of 30° . The results in Table 3 again indicate that the collapse loads predicted by the new procedure are not particularly sensitive to the mesh refinement. The predictions for coarse mesh 4, which has 200 triangles and 285 velocity discontinuities, are of similar accuracy to the predictions from fine mesh 4, which has 800 triangles and 1170 velocity discontinuities. Indeed, comparing the results from both meshes for the 24-plane approximation to the yield surface, we see that the fine mesh only reduces the collapse load error from 8.5% to 5.4% but

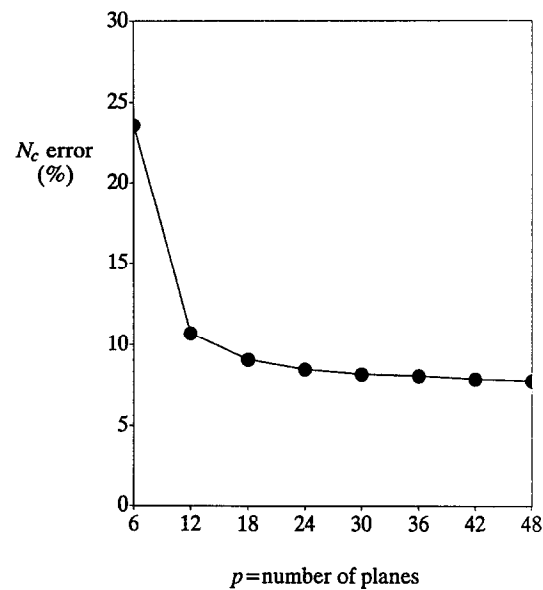


Fig. 12. Effect of yield surface linearisation on collapse load error (coarse mesh 4, smooth rigid strip footing on cohesive-frictional soil).

leads to a thirty-fold increase in CPU time. By taking advantage of the known form of the Prandtl collapse mechanism, the accuracy of the solutions could be further enhanced by arranging the elements in a log-spiral fan around the edge of the footing. Indeed, as with the Tresca case, the exact solution could be approximated very closely by placing the elements in a pattern which permits the Prandtl collapse mechanism to be reproduced.

The effect of not including velocity discontinuities in the analysis is shown in the results of Table 5. These were obtained using the meshes of Fig. 13, which are identical to the meshes of Fig. 11 except that no velocity discontinuities are included at all common edges between triangles. The error in the collapse load predictions, although larger than for the purely cohesive footing case, follows a similar pattern. The errors range from 99.1%, for coarse mesh 5 with a crude approximation to the yield surface, to 21.4%, for fine mesh 5 with a refined approximation to the yield surface. Comparing the results of Tables 4 and 5, the extra cost incurred by the inclusion of discontinuities in the upper bound formulation, although significant, is again balanced by the increase in the accuracy of the limit load. For the coarse mesh with a 24-plane linearisation of the yield surface, for example, the three and a half-fold increase in CPU time is rewarded by a five-fold reduction in the collapse load error.

The velocity fields for the fine mesh analyses with and without velocity discontinuities are shown, respectively, in Fig. 14 and 15. Despite the fact that the mesh with the discontinuities only gives a 5.4% error in the collapse load, its velocity field does not match the Prandtl failure mechanism precisely. The

Table 5
Results for smooth rigid strip footing on cohesive-frictional layer (no velocity discontinuities)

Mesh	p	m	n	i	t (s)	N_c	N_c error (%)
Coarse mesh 5	6	1432	640	573	32.1	60.00	99.1
Fine mesh 5	6	5662	2477	3269	843	49.21	63.3
Coarse mesh 5	12	2632	640	765	44	46.73	55.0
Fine mesh 5	12	10462	2477	4463	1175	38.71	28.4
Coarse mesh 5	24	5032	640	1194	80	43.13	43.1
Fine mesh 5	24	20062	2477	6728	2176	36.60	21.4

p = number of planes in linearised yield surface, m = number of rows in constraint matrix, n = number of columns in constraint matrix, i = number of iterations to solve LP, t = CPU time for SUN IPX with f77-O4.

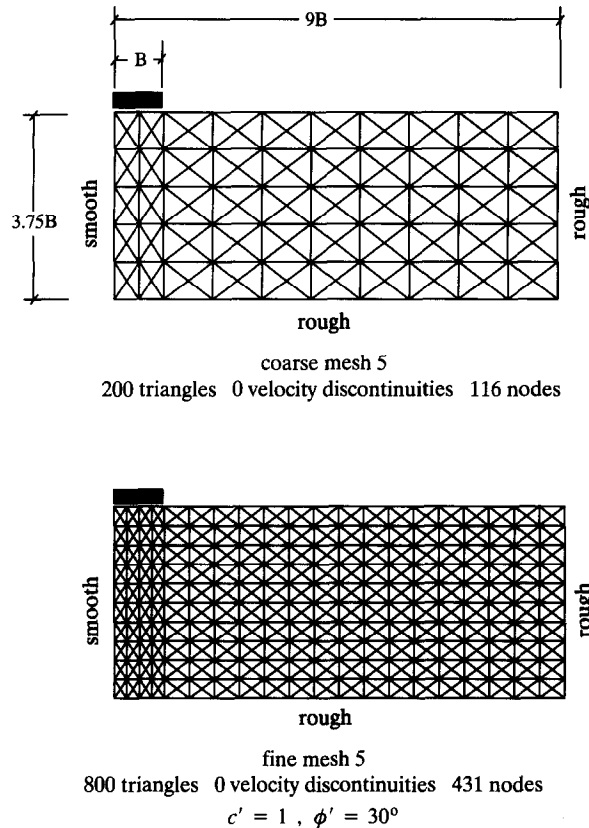


Fig. 13. Meshes for smooth rigid strip footing on cohesive-frictional soil (no velocity discontinuities).

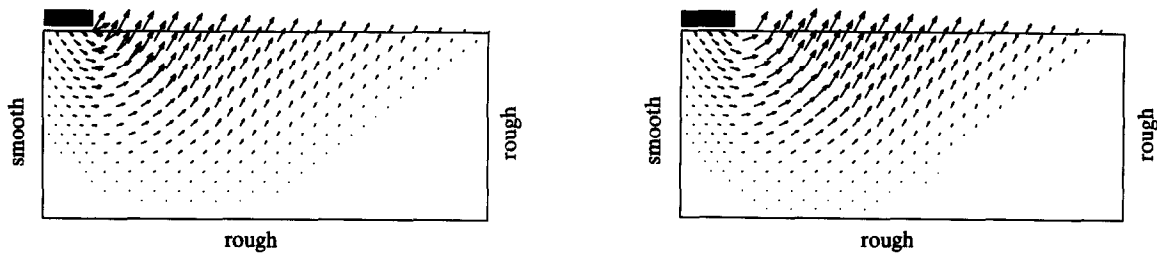


Fig. 14. Velocity vectors for smooth rigid strip footing on cohesive-frictional soil (fine mesh 4, velocity discontinuities, $p = 24$).

Fig. 15. Velocity vectors for smooth rigid strip footing on cohesive-frictional soil (fine mesh 5, no velocity discontinuities, $p = 24$).

velocity field for the grid without the discontinuities is clearly more constrained, particularly close to the edge of the footing where little vertical deformation takes place.

5. Conclusions

A new procedure for performing upper bound limit analysis using finite elements and linear programming has been described. The formulation permits large numbers of discontinuities in the velocity field and gives accurate upper bounds for both drained and undrained analysis. The technique improves existing finite element formulations of the upper bound theorem, which can only admit limited numbers of velocity discontinuities with specified signs of shearing.

Acknowledgments

The research reported in this paper was funded by a grant from the Australian Research Council. The authors are grateful for this support and would also like to thank Professor I.F. Collins for his stimulating discussions on plasticity theory.

Appendix

Consider the velocity discontinuity shown in Fig. 3. For this element, the power dissipated by plastic shearing is found by integrating the assumed value of the tangential velocity jump along the length of the discontinuity l according to

$$P_d = c \int_l (u^+ + u^-) dl$$

This may be equated to the power dissipated by the correct tangential velocity jump $|(u^+ - u^-)|$ for the same discontinuity in a soil with some unknown cohesion c^* according to

$$c^* \int_l |u^+ - u^-| dl = c \int_l (u^+ + u^-) dl \quad (42)$$

Now, since the quantities u^+ and u^- are constrained to be non-negative on l , it follows that

$$\int_l |u^+ - u^-| dl \leq \int_l (u^+ + u^-) dl \quad (43)$$

and hence

$$c^* \geq c \quad (44)$$

Note that $c^* = c$ when either $u^+ = 0$ or $u^- = 0$ on l , and corresponds to the case when the assumed tangential velocity jump is equal to the correct tangential velocity jump.

Using Eq. (21), a similar integration for the normal velocity jump along l furnishes

$$\tan \phi^* \int_l |u^+ - u^-| dl = \tan \phi \int_l (u^+ + u^-) dl \quad (45)$$

where this time the correct tangential velocity jump $|(u^+ - u^-)|$ is assumed to occur in the same discontinuity but with some unknown friction angle ϕ^* . Eq. (43) immediately supplies the result that

$$\tan \phi^* \geq \tan \phi \quad (46)$$

with the equality occurring under the same circumstances as before.

The final relation is obtained by dividing (42) by (45) to give

$$c^* \cot \phi^* = c \cot \phi \quad (47)$$

Eqs. (44), (46) and (47) imply that modelling the absolute value of the tangential velocity jumps using $(u^+ + u^-)$, instead of the correct value of $|(u^+ - u^-)|$, is equivalent to finding a rigorous upper bound for a soil whose discontinuity strength is given by c^* and ϕ^* , where $c^* \geq c$, $\phi^* \geq \phi$ and $c^* \cot \phi^* = c \cot \phi$. This confirms that the new formulation provides solutions which are rigorous upper bounds for a soil whose strength parameters are c and ϕ .

References

- [1] E. Anderheggen and H. Knopfel, Finite element limit analysis using linear programming, *Int. J. Solids Struct.* 8 (1972) 1413–1431.

- [2] A. Bottero, R. Negre, J. Pastor and S. Turgeman, Finite element method and limit analysis theory for soil mechanics problems, *Comput. Methods Appl. Mech. Engrg.* 22 (1980) 131–149.
- [3] S.W. Sloan, Lower bound limit analysis using finite elements and linear programming, *Int. J. Numer. Anal. Methods Geomech.* 12 (1988) 61–67.
- [4] S.W. Sloan, A steepest edge active set algorithm for solving sparse linear programming problems, *Int. J. Numer. Methods Engrg.* 26 (1988) 2671–2685.
- [5] S.W. Sloan, Upper bound limit analysis using finite elements and linear programming, *Int. J. Numer. Anal. Methods Geomech.* 13 (1989) 263–282.
- [6] J.C. Nagtegaal, D.M. Parks and J.R. Rice, On numerically accurate finite element solutions in the fully plastic range, *Comput. Methods Appl. Mech. Engrg.* 4 (1974) 153–177.
- [7] H.S. Yu, S.W. Sloan and P.W. Kleeman, A quadratic element for upper bound limit analysis, *Engrg. Comput.* 11 (1992) 195–212.
- [8] S.W. Sloan, A. Assadi and N. Purushothaman, Undrained stability of a trapdoor, *Geotechnique* 40 (1990) 45–62.
- [9] A. Assadi and S.W. Sloan, Undrained stability of a shallow square tunnel, *J. Geotech. Div. ASCE* 117 (1991) 1152–1173.
- [10] S.W. Sloan and A. Assadi, Undrained stability of a square tunnel in a soil whose strength increases linearly with depth, *Comput. Geotech.* 12 (1991) 321–346.
- [11] J.K. Reid, FORTRAN subroutines for handling sparse linear programming bases, Report R8269, AERE Harwell, 1976.
- [12] J.K. Reid, A sparsity exploiting variant of the Bartels–Golub decomposition for linear programming bases, *Math. Program.* 24 (1982) 55–69.
- [13] D. Goldfarb and J.K. Reid, A practicable steepest-edge simplex algorithm, *Math. Program.* 12 (1977) 361–371.